


Article

Automatic Detection of Regional Snow Avalanches with Scattering and Interference of C-band SAR Data

Jinming Yang ¹, Chengzhi Li ^{1,2}, Lanhai Li ^{3,4,5} , Jianli Ding ^{1,2}, Run Zhang ⁶, Tao Han ⁷ and Yang Liu ^{3,4,5,*}

¹ College of Resources and Environment Science, Xinjiang University, Urumqi 830046, China; yjm@stu.xju.edu.cn (J.Y.); xdlichengzhi@xju.edu.cn (C.L.); watarid@xju.edu.cn (J.D.)

² Institute of Arid Ecological Environment, Xinjiang University, Urumqi 830046, China

³ State Key Laboratory of Desert and Oasis Ecology, Xinjiang Institute of Ecology and Geography, Chinese Academy of Sciences, Urumqi 830011, China; lilh@ms.xjb.ac.cn

⁴ Ili Station for Watershed Ecosystem Research, Chinese Academy of Sciences, Xinyuan 835800, China

⁵ Research Center for Ecology and Environment of Central Asia, Chinese Academy of Sciences, Urumqi 830011, China

⁶ Key Laboratory of Tibetan Environment Changes and Land Surface Processes, Institute of Tibetan Plateau Research, Chinese Academy of Sciences (CAS), Beijing 100101, China; zhangrun@itpcas.ac.cn

⁷ The Seventh Detachment of the Special Police, Urumqi Public Security Bureau, Urumqi 830017, China; ht_dsslab@163.com

* Correspondence: liuyang@ms.xjb.ac.cn; Tel.: +86-181-2930-2998

Received: 29 June 2020; Accepted: 25 August 2020; Published: 27 August 2020



Abstract: Avalanche disasters are extremely destructive and catastrophic, often causing serious casualties, economic losses and surface erosion. However, far too little attention has been paid to utilizing remote sensing mapping avalanches quickly and automatically to mitigate calamity. Such endeavors are limited by formidable natural conditions, human subjective judgement and insufficient understanding of avalanches, so they have been incomplete and inaccurate. This paper presents an objective and widely serviceable method for regional auto-detection using the scattering and interference characteristics of avalanches extracted from Sentinel-1 SLC images. Six indices are established to distinguish avalanches from surrounding undisturbed snow. The active avalanche belts in Kizilkeya and Aktep of the Western TianShan Mountains in China lend urgency to this research. Implementation found that smaller avalanches can be consistently identified more accurately in descending images. Specifically, 281 and 311 avalanches were detected in the ascending and descending of Kizilkeya, respectively. The corresponding numbers on Aktep are 104 and 114, respectively. The resolution area of single avalanche detection can reach 0.09 km². The performance of the model was excellent in all cases (areas under the curve are 0.831 and 0.940 in descending and ascending of Kizilkeya, respectively; and 0.807 and 0.938 of Aktep, respectively). Overall, the evaluation of statistical indices are POD > 0.75, FAR < 0.34, FOM < 0.13 and TSS > 0.75. The results indicate that the performance of the innovation proposed in this paper, which employs multivariate comprehensive descriptions of avalanche characteristics to actualize regional automatic detection, can be more objective, accurate, applicable and robust to a certain extent. The latest and more complete avalanche inventory generated by this design can effectively assist in addressing the increasingly severe avalanche disasters and improving public awareness of avalanches in alpine areas.

Keywords: Sentinel-1A SLC; scattering and interference characteristics of avalanches; principal component analysis; support vector machine; machine learning; snow avalanche mapping

1. Introduction

Snow avalanche (hereinafter “avalanche”) is among the most catastrophic natural disasters worldwide and seriously threatens the safety of residents, socioeconomic development and biodiversity [1–5]. From the perspective of geoscience, erosion from avalanches causes the hazard-bearing bodies increasingly fragile, reshaping the micro-geomorphology and changing the type and density of surface cover, these effects will be more conducive to its re-release, thus forming a vicious circle [6]. Recently, frequent extreme snowfall events and the warming effect in mountainous areas have aggravated the avalanche hazard [7]. Poor decision-making and forecasting are the main causes of fatal avalanches. Therefore, there is an urgent need for avalanche spatial distribution mapping to provide more efficient support in coping with increasingly harsh avalanche hazards.

Different approaches have been employed to produce avalanche maps. Through field observation, some facts and data sets about avalanche activity are well-documented, providing a scientific basis for the rational use of mountain land and effective avalanche governance [8–11]. However, avalanches are ignored in areas without observation stations and inaccessible to observers [12], and this part of the data gap accounts for a substantial proportion. The sound wave detection method [13,14], the lake sediment method [15], and the tree-ring based avalanche reconstruction method [16] have been proposed to update the methods of original investigation methods, but they can only identify avalanches occurring at a local point or within a small range. The result is that there is still a need to obtain accurate avalanche data on a regional scale to fill the huge data hole.

The rapid development of remote sensing technology has yielded some cases of regional avalanches being successfully identified using visual interpretation methods [17], object-oriented classification methods [18] and change detection methods [19,20]. The clear differences in morphology and texture patterns between an avalanche and the surrounding undisturbed snow are the main clues for interpreting multispectral images. Even very small avalanches can be identified if the resolution is high enough, but especially when the multispectral characteristics of avalanches become blurred, subjective artificial interpretation may introduce significant errors. The object-oriented method uses a fuzzy algorithm classification to distinguish an avalanche from the undisturbed snow around it, but it is still inadvisable to rely heavily on subjective threshold settings in many segments [21]. The above methods can identify avalanches in large areas, although recognition accuracy is limited by clouds and terrain shadows in the images and human perception as well. To overcome the aforementioned disadvantages, some researchers try to capture avalanches by detecting the change in backscatter in active microwave images that are despite clouds and without daylight [22]. Currently, multiperspective exploration attempts have been carried out [23,24]. Even so, this is not applicable in complicated topography or areas with only sporadic small-scale avalanches. Actual observations reveal that the echo causing an increase in backscatter was not necessarily an avalanche—other features specific to the environment or complex qualitative changes in snow cover will also affect it. In addition to backscatter, the characteristics of avalanches have not been fully revealed, such as other scattering and interference properties. Therefore, a more objective, reliable and universal scheme to auto-detect avalanches on the regional scale must be innovated.

Machine-learning methods—with the advantages of fast processing of multidimensional data, automation, extraordinary generalization ability and reliability—have made significant contributions to many studies. Among these, the support vector machine (SVM) method—especially designed for binary classification problems—is the most widely used for accomplishing such tasks as assessment of landslides, flood sensitivity analyses, and crop identification. However, it has been seldom applied for avalanche research. SVM methods has been employed by only a few researchers to assess avalanche sensitivity in conjunction with topographic and climatic factors [25–27]. Nonetheless, judging the spatial distribution of avalanche sensitivity is too broad in the current form to effectively alleviate worsening avalanche disasters. Therefore, the performance of SVM machine learning for automatic detection of regional avalanches needs to be confirmed.

The western part of the TianShan Mountains in China is a region that is avalanche-prone and experiences frequent and clearly hereditary cyclical events [28]. Out of the urgent need for a systematic understanding of avalanches, since the 1960s, researchers at TianShan Avalanche Station of the Chinese Academy of Sciences (hereinafter “avalanche station”) have conducted a great deal of field investigations and essential information about the location, type, scale and path distribution of avalanches have been collected [29–32]. However, the quality and scope of artificial field investigation are essentially limited by the professionalism of personnel and natural conditions, so the accuracy and quantity of avalanche inventory are generally insufficient. Moreover, in the past 15 years, new construction of mountain transportation corridors, the extension of energy and communication lines, and the emergence of tertiary industry in the alpine mountains to accommodate winter sports have brought about increased peril of avalanches to humanity, economic development, cultural exchange and ecological conservation [33]. Furthermore, due to climate change and topographic evolution, historical record are no longer applicable to examine and assess the current situation, but the changing circumstances has not forced a new method of avalanche detection. Moreover, from the perspective of detected snow types, the research on continental dry and cold snow has not been paid attention to, and this type of snow is typical in the study area. Focusing on the significance of improving the accuracy of the avalanche data sets, innovatively exploring the scattering and interference characteristics of continental dry and cold snow, and balancing the contradiction between avalanche disaster and economic development of the mountain area, it is imperative to carry out automatic avalanche detection in the region.

To address increasingly severe avalanche disasters in a complex climate and social environment, having a complete avalanche map that is more meticulous in space is essential. This paper aims to mine the response characteristics of scattering and interference on Sentinel-1 SLC (Single Look Complex) images, to find a more robust and applicable regional automatic detection method on this basic, to support auxiliary decision-making for avalanche prevention. The main objectives of this research are: (1) mining the scattering and interference characteristics of continental dry and cold snow avalanches in the active microwave C-band; (2) using SVM machine-learning method to perform automatic mapping of avalanches; and (3) verifying the accuracy and evaluating the performance of the method.

2. Study Site

The present study targets avalanches on Kizilkeya and Aktep in the west TianShan Mountains in Yili Kazakh Autonomous Prefecture, Xinjiang Uygur Autonomous region, China (Figure 1), a vital location that figures prominently in the development and promotion of the Silk Road core economic belt and is a traffic focal point connecting Eurasia. Two critical national transport lines transit the depressions of these mountains—G217 on Kizilkeya and G218 on Aktep. Kizilkeya ($84^{\circ}18'–84^{\circ}29'E$, $43^{\circ}25'–43^{\circ}32'N$) is isolated by the east–west section of highway G217 and has a natural window connecting to the external environment to the northwest. G217 is closed annually from October to April because roads and tunnel portals are often buried by avalanches. Aktep ($84^{\circ}18'–84^{\circ}27'E$, $43^{\circ}14'–43^{\circ}17'N$) is located on the east line of G218, on the west is the main water vapor exchange exposure. The statistics and comparison of other detailed geographic information between the two places are shown in Table 1.

In winter, the two mountainous areas are influenced by distorted polar air masses with a warm and humid climate and abundant snowfall. Moreover, metamorphism makes the deep frost develop excessively in the snow layer. Due to unique topographic factors, the avalanche path is widely distributed. The superposition of all these unfavorable factors causes frequent avalanches. Documented avalanches always obstruct traffic (up to four months) and cause casualties (a total of more than 100 people) in Kizilkeya and Aktep, 1967–2020.

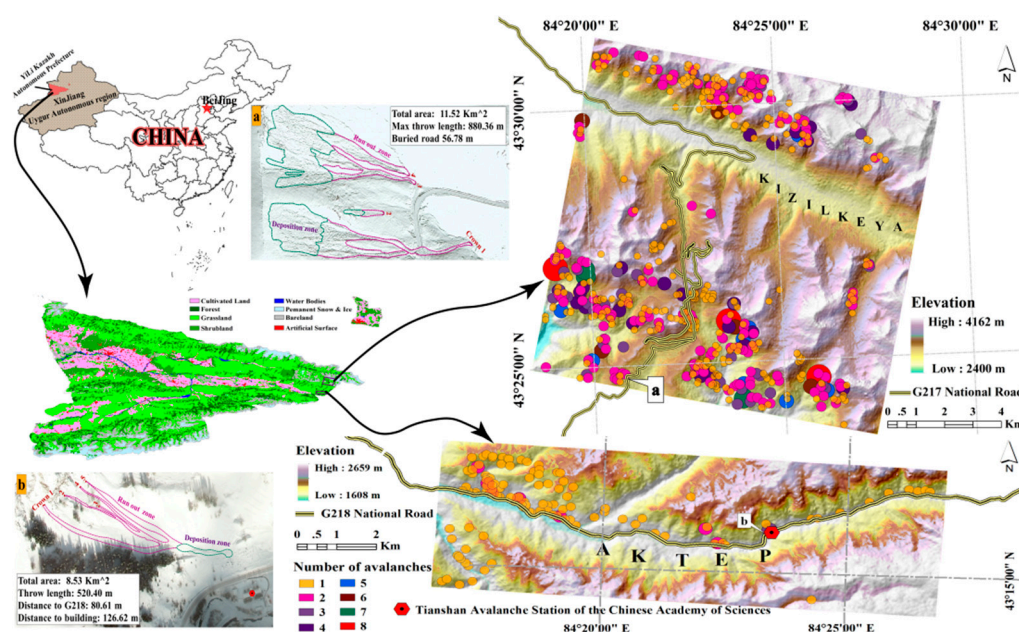


Figure 1. Schematic diagram of the study area. (a) Avalanche blocked the national highway G217; (b) avalanches threaten the safety of human life and appendages.

Table 1. Statistics of geographical attributes statistics for the implementation regions.

Characteristic	Kizilkeya	Aktep
Area	150.08 km ²	54.74 km ²
Elevation	2400–4162 m	1608–2659 m
Snowline	3700 m	3000 m
Forest line	2400 m	2800 m
Snow type	Continental dry cold snow	
Multiyear stable snow days	187 d	180 d
Average precipitation	339 mm/year	312 mm/year
Slope range	0°–79.31°	0°–74.08°
Number of avalanche paths	681	172
Avalanche type	trench-type, slope-type, groove-slope-type, slab avalanches	trench-type, slope-type, groove-slope-type

3. Materials and Methodology

The materials and methodology used for automatic detection of regional avalanches can be summarized into (presented visually are shown in Figure 2): (1) Material acquisition and preparation. This includes acquiring and preprocessing Sentinel-1A SLC images and SuperView-1 images separately and conducting avalanche field surveys. Among them, the Sentinel-1A SLC image is used to extract the entropy, alpha, backscatter and coherence of avalanches and establish the corresponding indicators, which in turn are ΔH , $\Delta \alpha$, $\Delta \sigma_{VV}$, $\Delta \sigma_{VH}$, γ_{VV} and γ_{VH} . These indicators will be employed to automatically detect avalanches. The optical SuperView-1 image is used to generate a high-precision avalanche inventory map; (2) Identifying the characteristic variables ΔH , $\Delta \alpha$, $\Delta \sigma_{VV}$, $\Delta \sigma_{VH}$, γ_{VV} and γ_{VH} using the principal component analysis (PCA); (3) Avalanche mapping. Use SVM to learn the simplified variable data set, and then use the training model generated by the learning sample to automatically detect avalanches; (4) Verifying the model's performance. Take the avalanche inventory map derived from SuperView-1 as a reference to evaluate the performance of the model through statistical indicators.

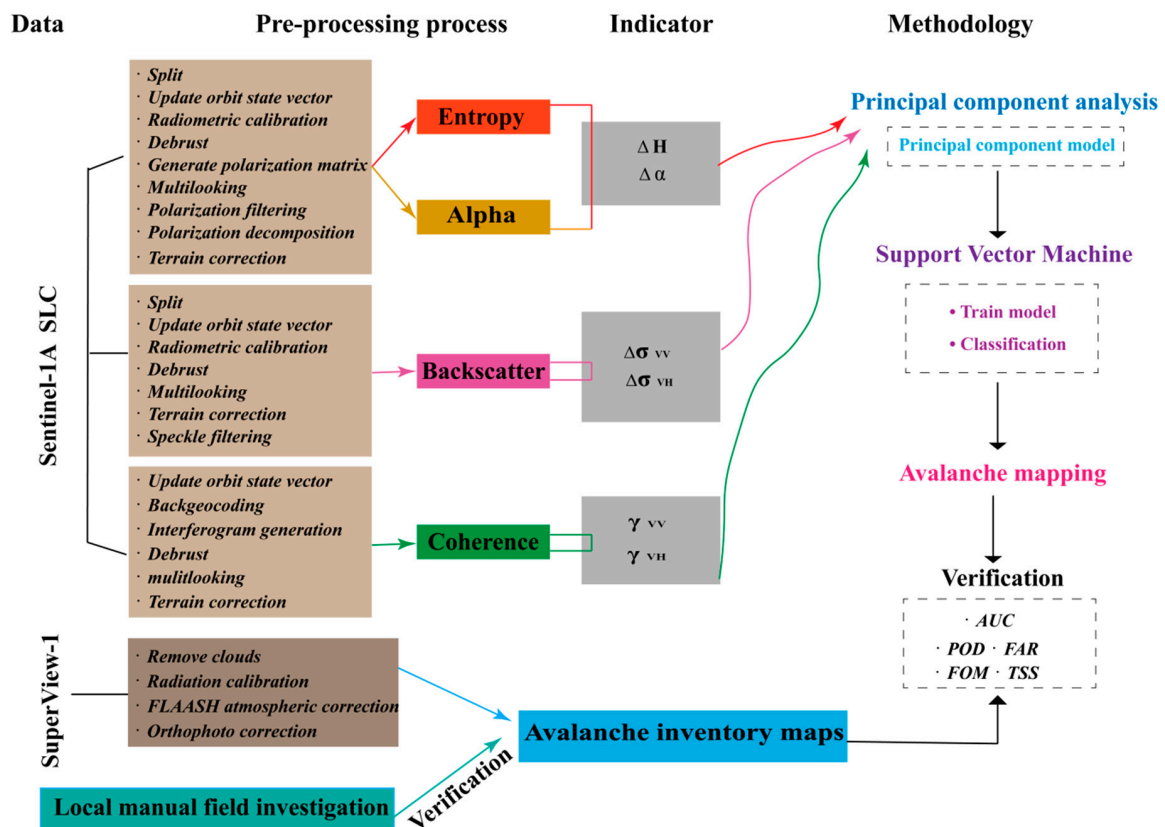


Figure 2. Schematic diagram of the overall workflow.

3.1. Sentinel-1 Image Acquisition and Processing

The Sentinel-1 satellite is specially designed for the Global environment and safety monitoring system (“Copernicus”) Project. In Kizilkeya and Aktep, only VV–VH polarized images (one image can cover the two study areas completely) in the IW (interferometric wide swath) mode are available. For this study, the SLC image with geo-reference, satellite attitude, and phase information is preferable between the two archived level-1 products of Sentinel-1A. A total of four Sentinel-1A SLC images were acquired for this study. It contains a pair of ascending orbit images and a pair of descending orbit images, and each pair of them includes a scene pre- and post-event conditions of avalanches (Table 2).

Table 2. Parameter statistics of collected Sentinel-1A SLC images.

Characteristic.	Ascending		Descending	
Dates	18 February 2019	9 October 2018	24 January 2019	8 October 2018
Slave/master	Master	Slave	Master	Slave
Track	12		165	
Width		250 km		
Ground resolution		5 × 20 m		
Baseline	124.536 m		79.657 m	

Sentinel-1A SLC image preprocessing:

- Split. The Sentinel-1A SLC image carries three sub-swath (IW1, IW2, IW3), while the study area is completely located in the IW2. Hence, only split IW2 for processing to reduce the computational burden;

- Orbital fine correction. Update the inaccurate information in the abstract meta data of the product with precision satellite position and velocity information which contained in POD (precise orbit determination) restituted orbit file;
- Radiation calibration. Typical SAR (synthetic aperture radar) data processing, which produces level-1 images, does not include radiometric corrections and significant radiometric bias remains. The significance of radiation correction is to make the pixel values of the SAR images truly represent the radar backscatter of the reflecting surface;
- Debrust. For the IW model SLC products, each sub-swath consists of a series of burst in azimuth. The individually focused complex burst data are included, in azimuth-time order, into a single sub-swath image, with black-fill demarcation in between. Debrust processing can eliminate black-fill demarcation by resampling and merging;
- Multilooking. Average the resolution of the range and azimuth direction of the image, suppress the speckle noise of the image and improve the radiation resolution of the image. Number of range looks: 4. Number of azimuth looks: 1;
- Range Doppler terrain correction. The topographical variations of the scene and the tilt of the satellite sensor may distort the distance in the SAR image. Terrain correction makes the geometric representation of the image as close as to the real world. Map projection: WGS84;
- Speckle filtering. The Lee sigma filter method is used to remove the noise in the Sentinel-1 image caused by the random superposition of multiple scattering sources in space. Filter: Lee sigma. Target window size: 3×3 . Sigma: 0.9.

3.1.1. Generating Scattering Characteristics of Avalanche

Polarization decomposition breaks down the complex scattering of surface echoes into several single scattering processes, each corresponding to a specific scattering matrix [34]. H-alpha dual polarization decomposition breaks down Sentinel-1 images based on feature vectors and does not change with modifications of the antenna coordinate system, so the information of polarization entropy and scattering angle is more reliable. Based on the feature spaces of entropy (H) and alpha (α), surface, volume and multiple scattering components can be accurately extracted [35]. Entropy characterizes the degree of polarization of ground features; can be expressed as:

$$H = -\sum_{i=1}^2 p_i \log_2(p_i), \quad p_i = \lambda_i / \sum_{k=1}^2 \lambda_k \quad k = 1, 2 \quad (1)$$

Based on the backscatter mechanism, the H parameter can be regarded as the output of a stochastic calculation within a resolution unit. According to Equation (1), the range of H is 0–1. Random scattering works when H approaches 1. The system changes from simple isotropic scattering to completely random scattering when H is between 0 and 1. The types of ground objects recognized become fewer as H increases. Therefore, the use of H alone would be inadequate. Alpha can assist in recognition of the type of scattering mechanism and can be expressed as:

$$\alpha = \sum_{i=1}^2 p_i \alpha_i \quad (2)$$

When α approaches $\pi/4$, it represents the volume scattering component. When α is $\pi/2$, it denotes the multiple scattering component and when α is 0, it represents the surface scattering component.

The characteristic index of polarization entropy can be expressed as:

$$\Delta H = (H)^m - (H)^s \quad (3)$$

Alpha's characteristic index can be expressed as:

$$\Delta\alpha = (\alpha)^m - (\alpha)^s \quad (4)$$

In Equations (3) and (4), m is the master image and the transit time of the image starts after the avalanche; s is the slave image, which is before the avalanche.

In addition at the air–snow interface, snow's volume, depth, water equivalent, density and surface roughness change conspicuously after an avalanche. These changes will eventually be reflected by changes in the backscatter of the Sentinel-1 image [36], which can be expressed as:

$$\sigma^0(\text{dB}) = 10 \log_{10}(\text{abs}(\sigma^0)) \quad (5)$$

where σ^0 (dB) represents the backscatter image in dB and σ^0 represents the sigma naught image.

Two indices related to backscatter are created, namely $\Delta\sigma_{VV}$ and $\Delta\sigma_{VH}$. They can be expressed as:

$$\Delta\sigma_{VV} = (\sigma_{VV})^m - (\sigma_{VV})^s \quad (6)$$

$$\Delta\sigma_{VH} = (\sigma_{VH})^m - (\sigma_{VH})^s \quad (7)$$

3.1.2. Generating Interference Characteristics of Avalanche

The phase and intensity similarity of radar echo reflected by coherence and the similarity of target scatterers are the pivotal references for ground interpretation [37,38]. The coherence for a stack with the master image m is defined as:

$$\gamma = \frac{\sum_{i=1}^{Looks} (C_1 * C_2)}{\sqrt{\sum_{i=1}^{Looks} (|C_1|^2) \bullet \sum_{i=1}^{Looks} (|C_2|^2)}} \quad -1 \leq C \leq 1 \quad (8)$$

C_1 is one of the plural images. C_2 represents multiplication with the conjugate of another complex image. After the amplitudes are normalized separately, the range is from 0 to 1. The closer the phases of the two electromagnetic waves are or the more continuous the change is, the closer the value of the coherence coefficient is to 1 and the more similar the features are.

3.2. SuperView-1 Image Collection and Processing

The satellite SuperView-1 was launched in Taiyuan, Shanxi Province, China, at 11:23 on 28 December 2016. Images passing through Kizilkeya on 16 February 2019 and Aktep on 16 January 2019 (Table 3) were used to generate reliable records of the location, area, throw and type of avalanches in the corresponding areas. These avalanche occurrence inventory maps were utilized to verify the performance of the automatic detection method. Images were preprocessed by cloud removal, radiometric calibration, FLAASH atmospheric correction and orthophoto correction before interpretation and vectorization. Bühler proposed a detailed and logical visual interpretation scheme for avalanches [17]. In this paper, 473 and 124 avalanches on Kizilkeya and Aktep, respectively, yielded sophisticated delineations by learning from the convincing steps in his paper. In addition, the mixed pixels on the boundary are removed as much as possible to make it sharper.

Table 3. Parameter statistics of collected SuperView-1 images.

Characteristic		Kizilkeya	Aktep
Revisit period		1 d	
Resolution	multispectral	2 m	
	panchromatic	0.5 m	
Orbit height		530 km	
Width		12 km	
Side swing angle		0.56°	
Maximum image size		60 × 70 km	
Cloud content		1.2%	0.5%

The above data are from the WGS84 coordinate system, UTM N44 projection.

3.3. Local Manual Field Investigation

From 18–24 January 2019, an avalanche field survey was conducted along the G218 transport line, centering on the avalanche station. Details of the avalanche type, location, area and surrounding cover type were recorded. Moreover, the particle size, moisture content, density and depth of snow were measured strictly in accordance with the standards of the IACS (International Association of Cryosphere Science). Limited by harsh natural geographic and meteorological conditions, only 276 avalanche locations were recorded, which assisted for visual interpretation and mastering the local avalanche situation.

3.4. Methodology

3.4.1. Principal Component Analysis

PCA is a technique for exploring high-dimensional data structures [39]. Correlated high-dimensional variables can be synthesized into linearly independent low-dimensional variables by principal component analysis, thereby revealing the most consequential elements and structures hidden in intricate data [40].

The basic steps for performing PCA are as follows:

1. Perform Kaiser–Meyer–Olkin (KMO) and Bartlett spherical test on each index matrix [41]. Commonly used KMO metrics are given by Kaiser: above 0.9 = very suitable; 0.8 = suitable; 0.7 = moderate; 0.6 = not very suitable; below 0.5 = extremely unsuitable;
2. Standardization brings all indicators to a common platform with a mean of zero and a standard deviation of one;
3. Calculate the eigenvalues, corresponding eigenvectors, contribution rate and cumulative contribution rate of the covariance matrix. The component that satisfies the condition that the eigen value are greater than 1 and the cumulative contribution rate is more than 80% will be selected as the principal component [42];
4. Calculate the rotated factor loadings of PCs to obtain the linear combination of the principal components, thereby obtaining a comprehensive model.

3.4.2. Support Vector Machine

The SVM classifier—also called the optimal edge classifier—can mine the information by learning the rules and patterns of the data [43–45]. In this paper, a separating hyperplane is established by using the SVM to distinguish avalanches from undisturbed snow cover. To begin, data were cross-validated (folds = 5). Six kernel functions were used to learn sample data. The one with the highest accuracy of the six training model was selected according to the AUC (area under the curve of ROC) values. The larger the AUC value, the better the ability to detect avalanches in undisturbed snow. Subsequently,

the training area was used to classify the study site (the index matrix requiring normalization of the area to be classified).

3.4.3. Model Evaluation

Probability of detection (POD), free arm rate (FAR), frequency of missed (FOM) and true skill statistic (TSS) indicators were selected to verify the method's performance. POD was the ratio of the number of successfully identified avalanche events to the total number of avalanches that actually occurred. The value range was 0–1; the ideal state is 1.

$$POD = \frac{H}{H + M} \quad (9)$$

FAR indicates the ratio of events that are not actually an avalanche but classified as such.

$$FAR = \frac{FA}{H + FA} \quad (10)$$

FOM indicates the ratio of avalanche events not classified as such.

$$FOM = \frac{M}{H + M} \quad (11)$$

The range of FAR and FOM indicators is 0–1. As the value approaches 0, the more nearly perfect the state is. TSS is the difference between successful identification and misjudgment, it is used to comprehensively evaluate the total effect of automatic identification. The classification effect is better when $TSS = 1$; there is no classification technique when $TSS = -1$.

$$TSS = \frac{(H \times CN - FA \times M)}{(H + M)(FA + CN)} \quad (12)$$

In Equations (9)–(12), Hits (H) represents the pixels that were accurately identified. False alarm (FA) denotes pixels that were not actually avalanches but were misjudged as such. Misses (M) refers to pixels not correctly identified as avalanches. Correct negative (CN)) designated non-avalanche pixels that were accurately identified.

4. Results

4.1. Characteristics from Sentinel-1 Images of Avalanches

Compared with undisturbed snow, the occurrence of avalanches will simultaneously lead to an obvious increase in entropy, a sharp decrease in alpha, a moderate increase in backscatter and a slump in coherence. In Figure 3, the scattering and interference characteristics of avalanches are illustrated. The following statement makes a specific analysis and comparison of the ascending and descending in accordance with the order of entropy, alpha, backscatter and coherence.

The value of entropy (H) exhibits the distinguishing feature of increasing while the value of alpha (α) decreases in both ascending (Figure 3a) and descending (Figure 3b) images. Among them, the change of H is particularly obvious. In the ascending, the occurrence of an avalanche aggregates 50% H value from 0.42–0.69 to 0.84–0.91, which significantly increases (Figure 3c). The median position of avalanche H is much higher than that of undisturbed snow. The sharper and more concentrated change in the descending, from 0.25–0.41 to 0.88–0.94, is higher than that in the ascending during the same period (Figure 3d). Furthermore, in terms of the change of α , it has decreased, but the change in the descending (from 81.00°–86.00° to 54.00°–62.00°) is still greater than that in the ascending (from 70.00°–74.00° to 57.50°–63.00°)

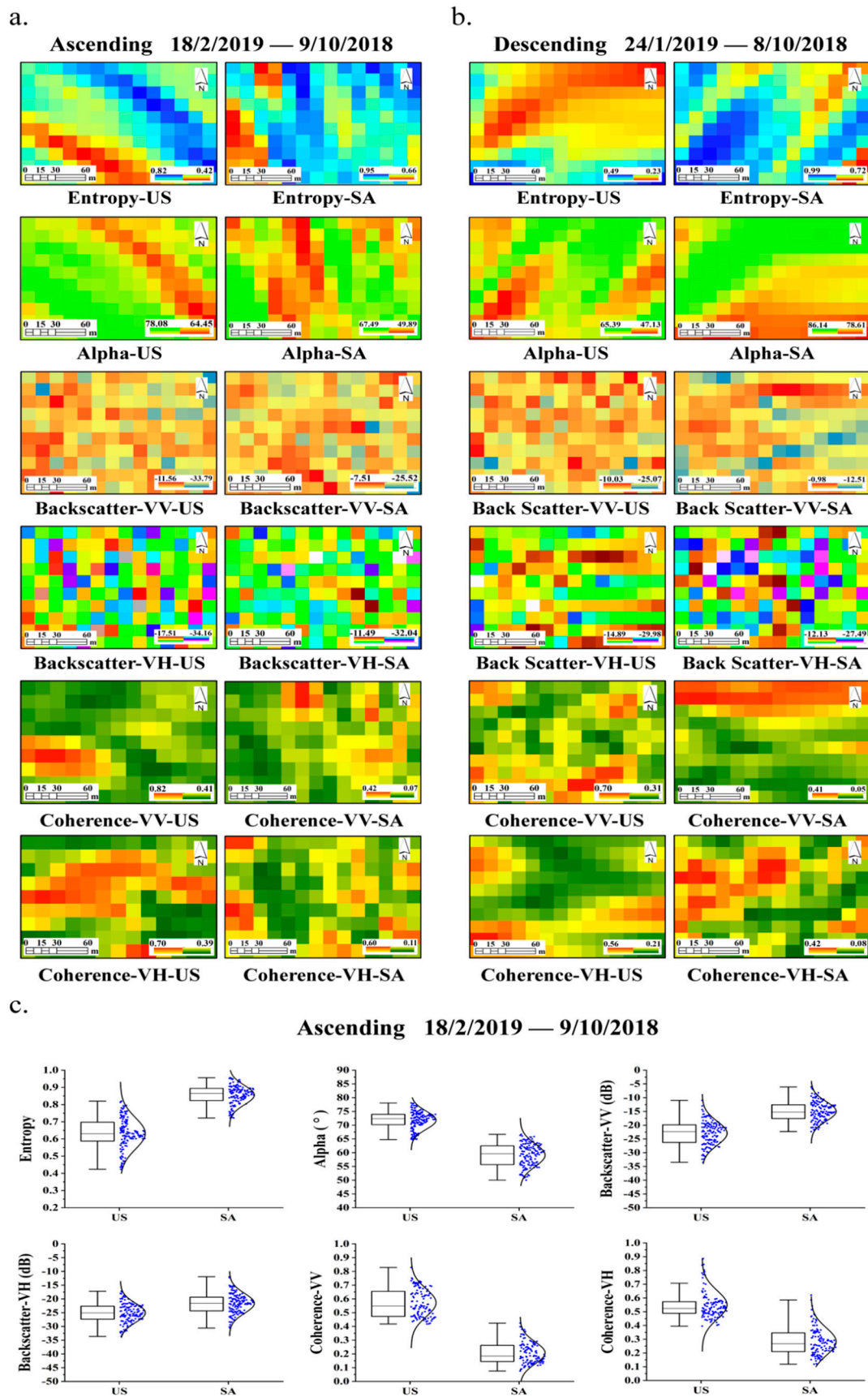


Figure 3. Cont.

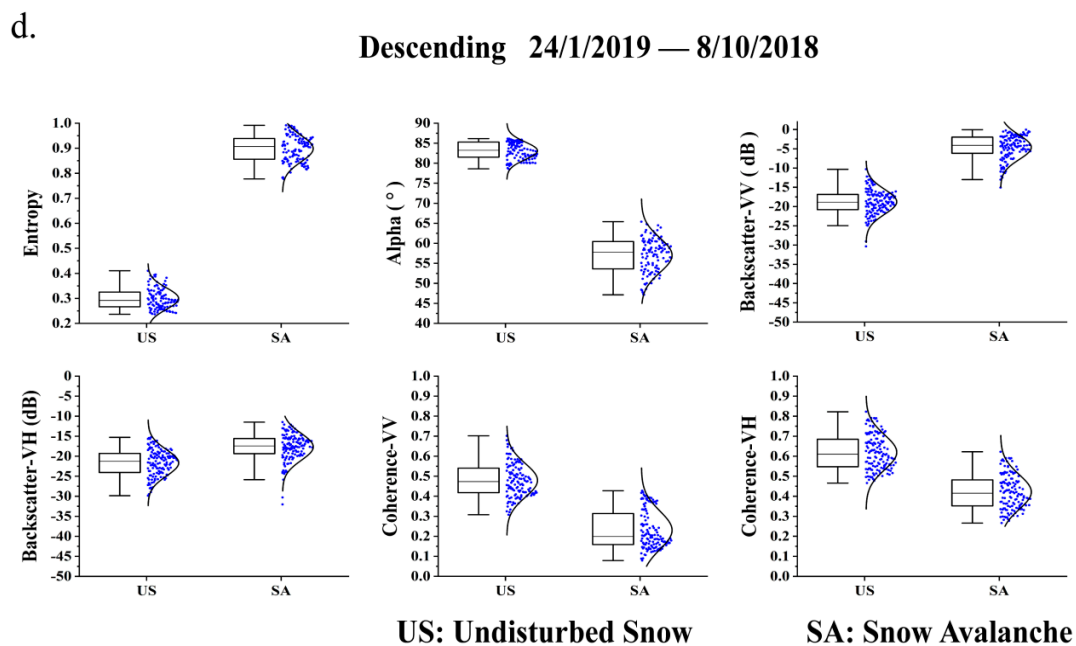


Figure 3. Scattering and interference characteristics of (a,b) avalanche and (c,d) boxplots.

The backscatter (σ) value of avalanche exhibits a marked increase in all cases, particularly dramatic in descending. In the VV polarization band of ascending, the value of σ after an avalanche increases from -26.0 – -19.5 to -17.0 – -12.5 dB, and the change in the descending is more overt, from -21.0 – -17.0 to -5.5 – -2.0 dB. In the VH polarization band, the variation is slightly less than that of the VV band, from -27.5 – -22.5 to -24.0 – -18.5 dB and from -26.0 – -19.0 to -19.0 – -14.0 dB, respectively.

The change in coherence (γ) is typical in all bands. In the polarization band of VV, the γ after avalanche drops in both ascending (from 0.48 – 0.65 to 0.14 – 0.25) and descending (from 0.41 – 0.54 to 0.17 – 0.32), and the median is fairly close to the lower quartile. The variation characteristics of γ in the polarization band of VH are similar to those of VV, but slightly weaker, from 0.49 – 0.57 to 0.20 – 0.33 and from 0.40 – 0.68 to 0.36 – 0.49 , respectively.

4.2. Generating Characteristic Variables

The results of the KMO and Bartlett spherical tests (Table 4) illustrate that the index matrix in all images is a positive definite matrix and suitable for principal component analysis. On **Kizilkeya**, the values of KMO are all greater than 0.8 (ascending = 0.824, descending = 0.871), with favorable suitability. The KMO value of Aktep (ascending = 0.707, descending = 0.747) is slightly lower than that of Kizilkeya, with moderate suitability.

Table 4. Statistics of Kaiser–Meyer–Olkin (KMO) and Bartlett test results.

KMO Sampling Suitability			Bartlett Sphericity Test		
			Approximate Chi-Squared	Degrees of Freedom	Significance
Kizilkeya	Ascending	0.824	461.164	21	0.000
	Descending	0.871	973.434	10	0.000
Aktep	Ascending	0.707	131.354	36	0.000
	Descending	0.747	129.047	28	0.000

Following the criteria in Section 3.4.1 for selecting principal components, two principal components were extracted from the ascending of Kizilkeya and three from the descending. Taking variables of

88.86% and 91.62%, respectively, of the total variability, especially the first principal component in the ascending image can even be interpreted as 57.26%. On Akteş's ascending orbit, two linear combinations are used to explain 82.01% of the total information, and in descending, three linear combinations explain 87.67% variables; their first principal component basically account for about half the content (56.65% and 42.81%, respectively, Table 5).

Table 5. Eigenvalues of the correlation matrix and its cumulative contribution rate.

Components	Kizilkeya				Akteş			
	Ascending		Descending		Ascending		Descending	
	Eigen Values	Cumulative Variance	Eigen Values	Cumulative Variance	Eigen Values	Cumulative Variance	Eigen Values	Cumulative Variance
1	3.436	57.26%	2.720	45.33%	3.383	56.38%	2.531	42.18%
2	1.580	88.86%	1.690	73.51%	1.538	82.01%	1.640	69.52%
3	0.575	93.18%	1.087	91.62%	0.959	97.99%	1.089	87.67%
4	0.235	97.10%	0.310	96.77%	0.091	99.51%	0.610	97.83%
5	0.141	99.45%	0.185	99.85%	0.030	100.00%	0.126	99.93%
6	0.033	100.00%	0.008	100.00%	0.000	100.00%	0.004	100.00%

The rotated factor loadings of the PCs are shown in Table 6. The difference in the contribution of each index to the principal component is obvious (major loadings for each item are in bold). In the ascending of Kizilkeya, the explanation of each index by PC1 is decidedly sufficient, which reflects the information of all indicators. Relatively speaking, the PC2 explanation is slightly inferior to that of PC1, in that the negative correlation with $\Delta\sigma_{VV}$ is only 0.174. The explanatory ability of principal components in descending order is PC1 > PC3 > PC2 of the descending orbit image. The indices with the strongest correlation are ΔH , $\Delta\sigma_{VH}$ and γ_{VH} , respectively. $\Delta\sigma_{VH}$, ΔH (in PC2) and ΔH (in PC3) are relatively less relevant to the principal components, respectively. In the ascending of Akteş, aside from the explanatory power of the $\Delta\alpha$ index of PC1 not being satisfactory, the others are entirely sufficient, especially strong positive correlation with $\Delta\sigma_{VH}$. The explanatory capacity of PC2 to each index is similar, which is no more than 0.67 and especially the correlation with $\Delta\sigma_{VH}$ which is minor. In the descending, the explanatory capacity of PC1 is similar to that of PC2, and the correlation between PC3 and other indices is less than 0.97, except for $\Delta\sigma_{VV}$.

Table 6. Rotated factor loadings of PCs.

Indicators	Kizilkeya					Akteş				
	Ascending		Descending			Ascending		Descending		
	PC1	PC2	PC1	PC2	PC3	PC1	PC2	PC1	PC2	PC3
ΔH	0.660	0.366	0.824	−0.002	−0.120	0.825	0.469	0.962	0.158	−0.065
$\Delta\alpha$	0.828	−0.420	0.776	0.566	0.150	−0.068	0.482	−0.811	0.223	−0.025
$\Delta\sigma_{VV}$	0.948	−0.174	−0.871	0.344	0.127	0.785	0.616	0.088	0.266	0.960
$\Delta\sigma_{VH}$	0.807	0.361	0.196	0.905	0.332	0.975	0.035	0.858	0.461	−0.097
γ_{VV}	−0.425	0.797	−0.780	0.266	0.143	0.690	−0.666	−0.451	0.826	−0.086
γ_{VH}	−0.763	−0.418	0.180	−0.602	0.777	0.808	−0.511	−0.019	0.949	−0.131

Principal component model of Kizilkeya:

$$SA_{Ascending} = 0.30 \Delta H + 0.30 \Delta\alpha + 0.72 \Delta\sigma_{VV} + 1.33 \Delta\sigma_{VH} + 0.08 \gamma_{VV} - 1.70 \gamma_{VH} \quad (13)$$

$$SA_{Descending} = 0.23 \Delta H + 0.45 \Delta\alpha - 0.28 \Delta\sigma_{VV} + 0.80 \Delta\sigma_{VH} - 3.03 \gamma_{VV} + 0.13 \gamma_{VH} \quad (14)$$

Principal component model of Akteş:

$$SA_{Ascending} = 0.39 \Delta H + 0.08 \Delta\alpha + 0.75 \Delta\sigma_{VV} + 2.27 \Delta\sigma_{VH} + 2.70 \gamma_{VV} + 2.30 \gamma_{VH} \quad (15)$$

$$SA_{\text{Descending}} = 0.31 \Delta H - 0.25 \Delta \alpha + 0.31 \Delta \sigma_{VV} + 0.68 \Delta \sigma_{VH} + 0.72 \gamma_{VV} + 0.34 \gamma_{VH} \quad (16)$$

Through principal component analysis, the following conclusions are obtained: in Kizilkeya's ascending and descending images, the dominant index of contribution rate is $\Delta \sigma_{VH}$. In Aktep's ascending image, the main indices with high contribution rate are γ_{VV} , γ_{VH} and $\Delta \sigma_{VH}$, the corresponding indices in the descending are γ_{VV} and $\Delta \sigma_{VH}$.

4.3. Snow Avalanche Mapping

4.3.1. Case Study 1: Kizilkeya

The ability to identify small avalanches and avalanches in complex terrain is stronger in descending images (Figure 4). Specifically, 281 and 311 avalanches were identified in the ascending (Figure 4a) and descending (Figure 4b) of Kizilkeya, respectively. The minimum avalanche area that can be detected is 0.09 km², and the maximum is 83.40 km². In ascending, the overall range of avalanche throwing is from 25.40 m to 421.30 m, 59% of the range is between 132.60 m and 397.80 m. In descending, the throwing range is 77.50 m to 454.30 m, with the main concentration (60%) between 180.30 m and 218.20 m. Avalanches on Kizilkeya are unevenly distributed spatially in areas at altitudes of 2750 m to 3450 m with a slope of 25° to 50°. Most of them occur in the south and west of the Picea Schrenkiana forest in the north. According to US standards classifications for avalanche scale, avalanches in Kizilkeya are mainly small and medium—almost 96% are small. The proportion of small avalanches in the descending is greater than in the ascending orbit.

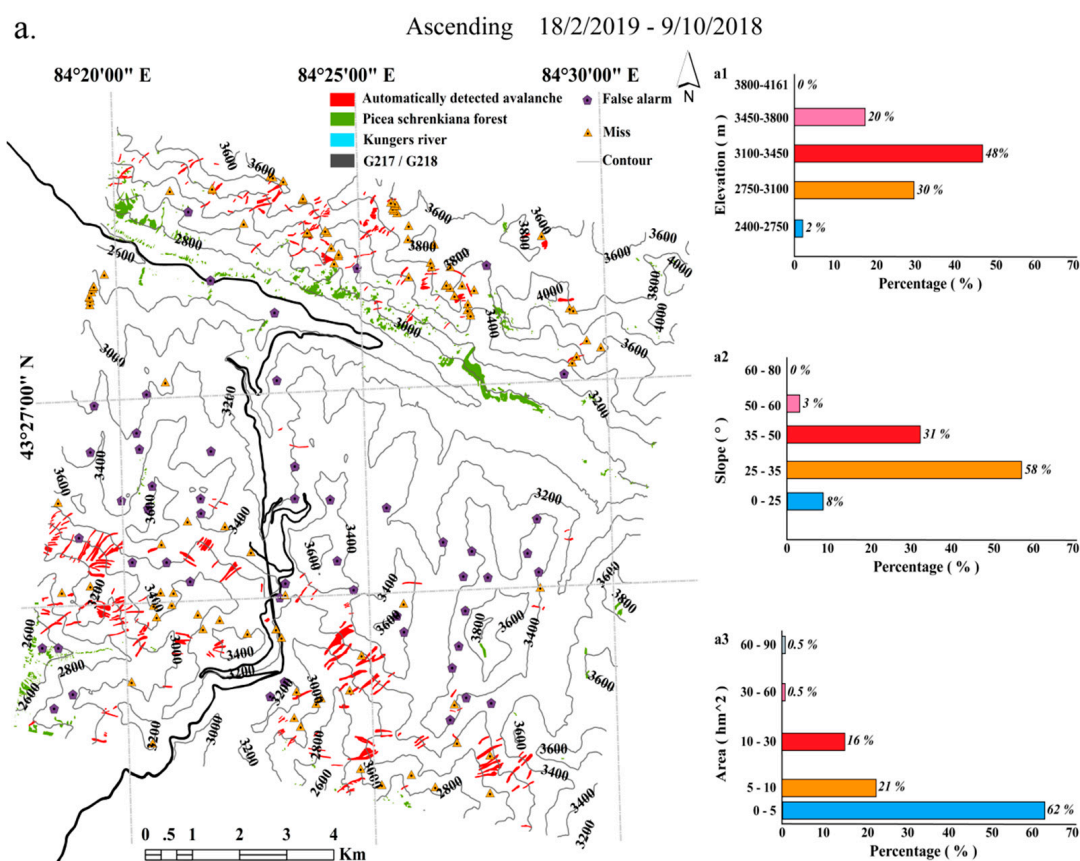


Figure 4. Cont.

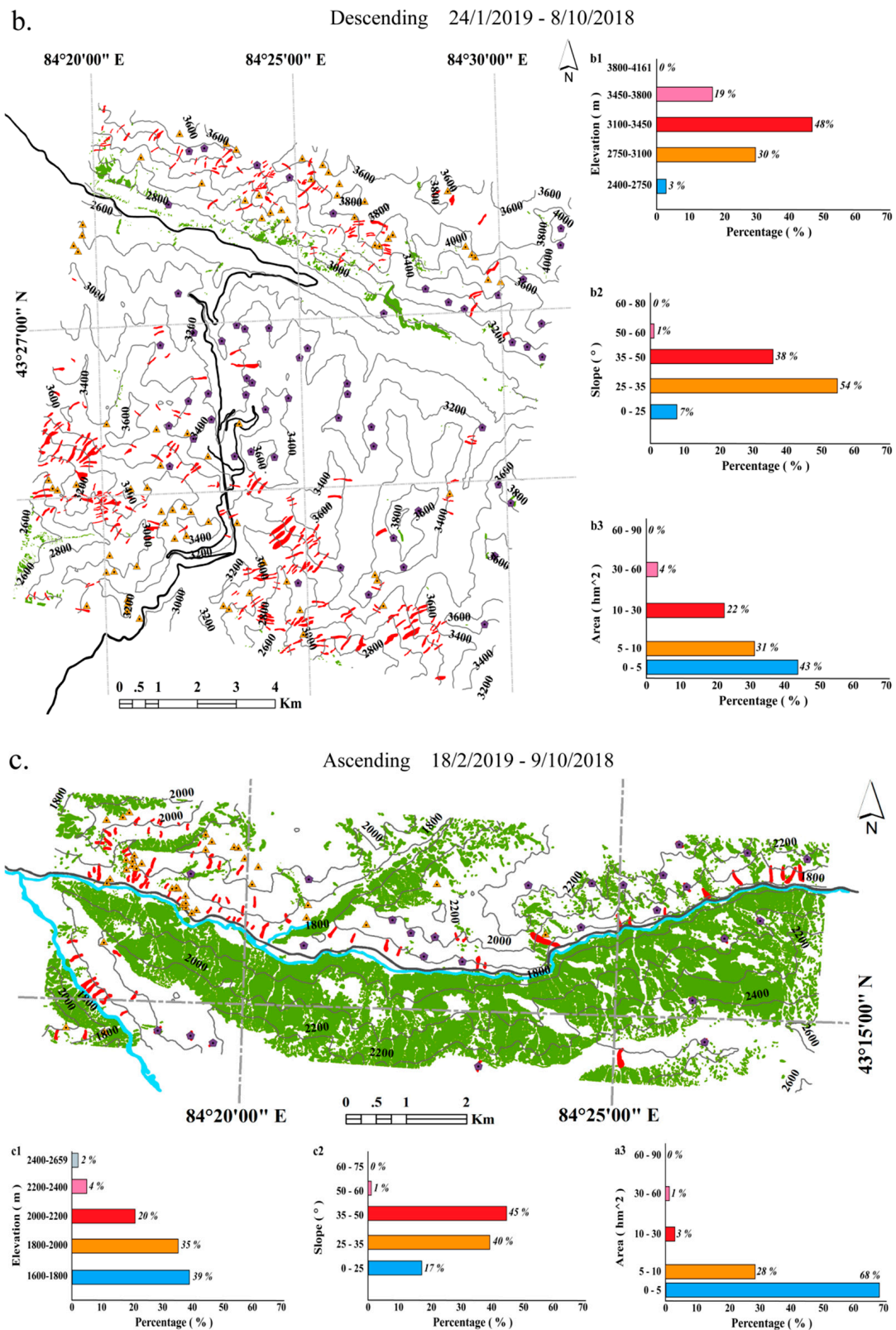


Figure 4. Cont.

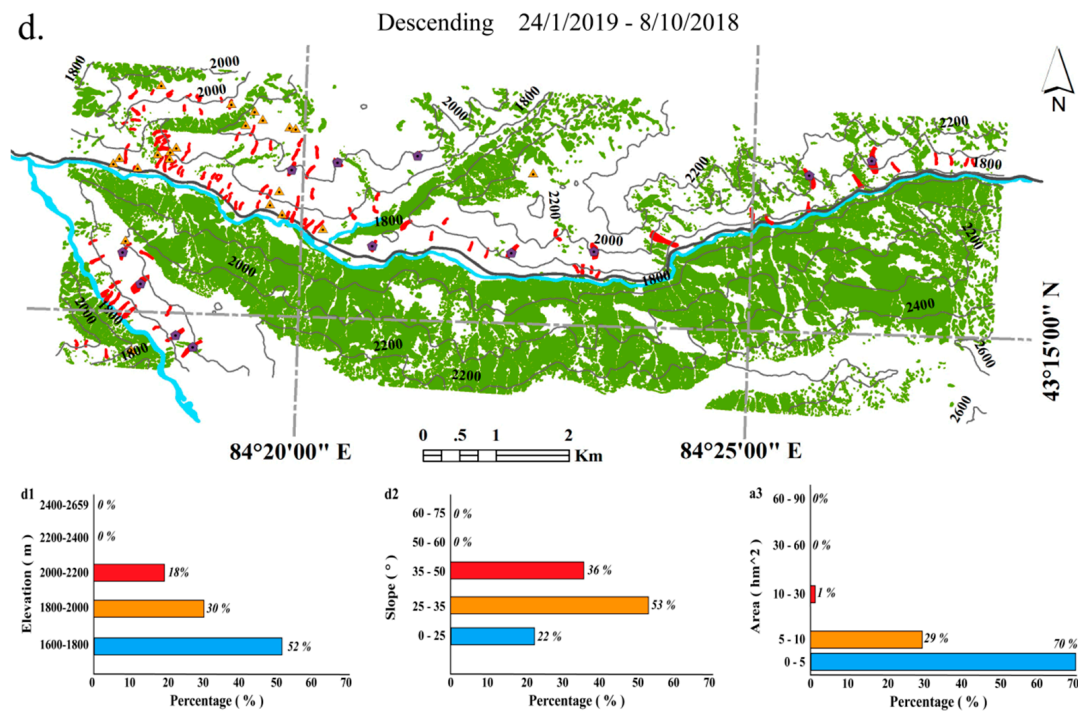


Figure 4. Snow avalanche mapping. (a,b) Kizilkeya; (c,d) Aktep.

4.3.2. Case Study 2: Aktep

In ascending (Figure 4c) and descending (Figure 4d), 104 and 111 avalanches are identified, respectively, on Aktep. The minimum and maximum resolutions by areas are 0.16 km² to 32.25 km². The extreme values of avalanche throw in the ascending are from 35.40 m to 424.20 m. Of the avalanche throw, 37% is between 155.43 m and 262.90 m. The corresponding values in the descending are 47.2 m and 441.9 m, mainly (40%) distributed between 80.40 m and 300.74 m. Avalanches are distributed horizontally in space, mainly along the G218 transport line and in the southwest near the Kungers river, especially in terrain with 25° to 50° slope at an altitude of 1600 m to 2000 m and 99% are small avalanches.

Overall, avalanches can be automatically detected in both ascending and descending of Sentinel-1A SLC images. However, due to the opposite orbital position of the satellite when scanning the surface, coupled with the role of the topography of the study area, the descending image is more conducive to capturing the characteristics of the avalanche and can always identify more and finer avalanches, especially in the rugged terrain. In addition, avalanches are not evenly distributed. There are almost none in the plains and in the *Picea Schrenkiana* forest areas. Avalanches occur frequently on slopes, in trenches and in areas with steep terrain along the fjords. They are active along the G217 and G218 lines that directly abut human property.

In terms of morphology, most avalanche accumulation areas are in the form of single or multiple “tongues”; some are irregular. Thus, there are generally no obvious morphologic features.

4.4. Verification

4.4.1. AUC

The samples were sequentially trained based on the six kernel functions in the SVM. In all four cases, classification accuracy based on Gaussian SVM kernel function is the highest, and the AUC is more than 0.93, with only a slight difference (Figure 5). The inflection point at which the Kizilkeya data (Figure 5a), can satisfy the minimum FPR (False Positive Rate) while the TPR (True Positive Rate) remains relatively large appears closer to the (0, 1) point in the descending (0.19, 0.93) than in

the ascending (0.22, 0.79). The higher AUC value in the descending indicates more clearly that the performance of the model is better and has the most nearly perfect performance. The points with the largest absolute values of the sum of the horizontal and longitudinal coordinates of the curves in the Aktep (Figure 5 ascending and descending appear at (0.1, 0.51) and (0.05, 0.8), respectively, and the automatic recognition performance in the descending (AUC = 0.938) is obviously better than that in the ascending (AUC = 0.807). In summary, the automatic detection method has a potent discrimination ability for avalanche samples and is more potent in the descending image.

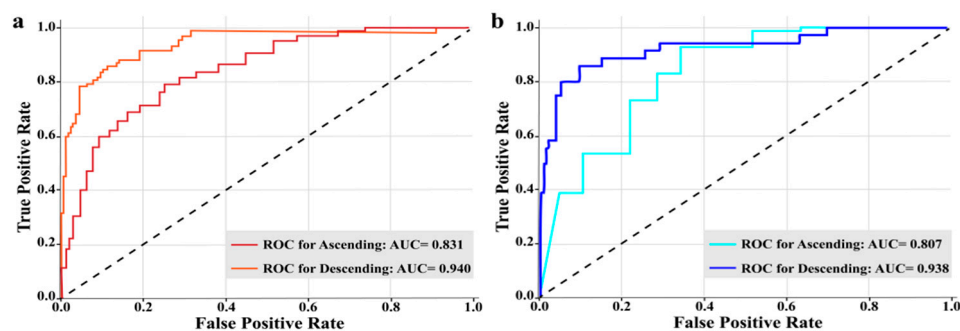


Figure 5. Area under the curve (AUC) of fine Gaussian support vector machine (SVM), (a) Kizilkeya; (b) Aktep.

4.4.2. Statistical Indicator

The effects of automatic identification of avalanches were evaluated by POD, FAR, FOM and TSS indicators (Table 7). The group of automatic recognition cases with the highest classification accuracy and the best comprehensive performance of the model is the descending of Aktep (POD = 0.924, FAR = 0.340, FOM = 0.076, TSS = 0.921). The statistical indicator values of 0.897 (POD), 0.109 (FAR), 0.103 (FOM) and 0.890 (TSS) were calculated for Aktep rank second in ascending, followed by Kizilkeya's descending, with values of 0.820 (POD), 0.116 (FAR), 0.180 (FOM) and 0.818 (TSS), respectively. The Kizilkeya ascending values of 0.754 (POD), 0.139 (FAR), 0.246 (FOM) and 0.751 (TSS) rank last.

Table 7. Statistics for model evaluation.

Statistics	Evaluation Index							
	Kizilkeya				Aktep			
	POD	FAR	FOM	TSS	POD	FAR	FOM	TSS
Ascending	0.754	0.139	0.246	0.751	0.897	0.109	0.103	0.890
Descending	0.820	0.116	0.180	0.818	0.924	0.340	0.076	0.921

The results demonstrate that more avalanches can be correctly identified in the descending image; which is also more advantageous for identifying small avalanches. To sum up, the results of descending image recognition are more reliable. Missed avalanches are mainly small avalanches in mountainous areas with large terrain fluctuations and narrow trenches, as well as some dry avalanches.

5. Discussion

5.1. Impact of Source Image Availability

The potential of optical remote sensing images for avalanche mapping is being tapped. QuickBird's multispectral band [18], Landsat 8's panchromatic band [23] and SPOT's near-infrared band [17] have been verified to identify avalanches. In this study, the optical images of many sensors were considered, although, most images were not useful. Few satellites transit over the study area, and the accuracy of their images is insufficient. Because the avalanche types distributed in these two mountain areas are

generally small, only when the spatial resolution of the image reaches the centimeter level can it be accurately interpreted. Some images have high spatial and temporal resolution, while large areas of the surface are obscured by clouds and shadows. Some satellites do not even scan across the study area. SuperView-1 images are available, but only one scene image is available in each area. Therefore, it is difficult to find optical remote sensing images to identify avalanches on a large scale.

The Sentinel-1 C-band SAR is not affected by cloud and rain, can work at night, has a high spatio-temporal resolution and can collect global data. These performance advantages over optical imaging make it more suitable for detecting avalanches. Malnes and Eckerstorfer et al. used the significant differences in the backscatter of avalanches and undisturbed snow to perform automatic avalanche identification. However, the FPR can be increased by some features with backscatter variation characteristics as those of to avalanches [22]. For example, Wesselink misidentified two glaciers as avalanches when identifying avalanches in the Svalbard area [46]. Eckerstorfer also misidentified agricultural land and glaciers with backscatter variation characteristics similar to avalanches [47]. Therefore, monitoring avalanches based on backscatter changes alone is inadequate and inapplicable.

Based on previous research, the significance of establishing multivariate comprehensive avalanche detection is recognized. The scattering and interference response to avalanche can be fully extracted and analyzed using Sentinel-1 SLC images. As shown in Figure 6, avalanches caused changes in the scattering mechanism to occur mainly in the low-entropy surface scattering (Z1) region, the surface scattering (Z4) region and the high-entropy scattering (Z8) region. Overall, the scattering angle decreases as the scattering randomness increases. Snow is typically a dense medium. Therefore, multiple near-field scattering must be considered to accurately determine its scattering characteristic parameters. Many studies have illustrated that bulk scattering and underlying surface scattering of snow dominate the total echo. The underlying surface scattering that existed before and after the avalanche was removed when the ΔH and $\Delta\alpha$ indices were established. Thus, the surface of the avalanche becomes rough and bulk scattering is dominant. Avalanches also have special interference characteristics. Specifically, the snow during the avalanche quickly rolled down from the starting area and finally stopped in the accumulation area after passing through the beating area. The change in snow depth is very large in these three regions, which is enough to affect the phase information on the Sentinel-1 image, resulting in reduced coherence. Therefore, the undisturbed snow before the avalanche at the same location is weakly correlated with the avalanche.

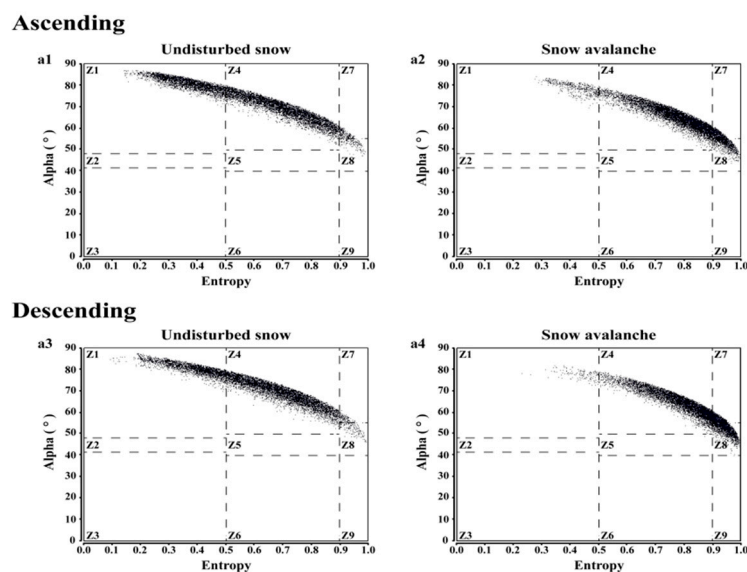


Figure 6. H- α space segmentation plot.

First, by thoroughly utilizing the information of avalanche characteristics in Sentinel-1 SLC images, the basis for identifying avalanches is no longer single, and the characteristics of avalanches can be interpreted more precisely and comprehensively. This has the advantage of obtaining complete and accurate avalanche data. Second, plus the excellent quality of the image itself has the potential to capture smaller and more well-defined avalanches on a larger scale.

5.2. Performance of the Automatic Avalanche Detection Method

Visual interpretation [17] and object-oriented classification methods [18,48] have been used by many researchers to identify avalanches in optical remote sensing images. Successful cases have been achieved in multispectral, panchromatic and near-infrared bands. In high-resolution SPOT images, the recognition accuracy can reach 71%, the false-negative rate is 16%, the false-positive rate of 11%. However, the accuracy is only 64% in shadow areas. Many clouds and shadows in the images have a significant impact on the results [17]. Meanwhile, there is still a strong anthropogenic subjectivity in the process of determining the starting point of the starting area, the end of accumulation area and the avalanche's boundary. In addition, using visual interpretation to identify avalanches is time-consuming and laborious. For example, Bühler's mapping of 18,737 avalanches over the entire 12,500 km² took approximately 600 h. Furthermore, using them is not effective in identifying avalanches in complex terrain. In this study, avalanche detection based on active microwave images that are not affected by clouds and all-day imaging can fundamentally avoid the influence of clouds and shadows. No additional data and threshold settings are involved in the whole operation. More important, the application of the SVM method to automatically detect avalanches avoids the intervention of human factors, making implementation of the method more objective, faster and robust.

Researchers have also used a change detection method to detect avalanches in images from the Sentinel-1 C-band active microwave. Vickers carefully defined the avalanche determination conditions based on the change detection method. He believes that a feature that satisfies the backscatter variation value of greater than six decibels and an area larger than 25 pixels may be an avalanche [49]. Although the interference of wet snow on the results was reduced by this method, some vegetation located in low-lying areas was misjudged. Moreover, the omission of small avalanches is very common. Eckerstorfer established a real-time system that automatically detects avalanches based on the study of Vickers. The maximum values of POD, FAR and TSS were 87.4%, 81.7% and 0.571 [47]. In this paper, the index values corresponding to his results were 92.4%, 34.0% and 0.921. Obviously, using the SVM machine-learning method to classify the avalanche has a higher POD and a lower FAR. Comparing results of TSS indicators further illustrates that the SVM machine-learning method is better in automatically identifying avalanches. Moreover, using artificially determined thresholds is unavoidable in the filtering and segmentation step of the process of identifying avalanches with the change detection method, but there is considerable human subjectivity involved. In contrast, the diversified avalanche characteristics established in this paper are capable of not only magnifying the avalanche features from regional data, but also thoroughly avoid the interference of human factors.

It is worth noting that level-1 SLC images are used in this paper and level-1 GRD (Ground Range Detected) images were used by Vickers, Eckerstorfer and Malnes. The large amount of data are the main reason for excluding SLC images. On the other hand, this means that the information provided by the SLC image will be more diverse; for example, the phase information is not included in the GRD image. The rich information in SLC images was important supporting data for establishing indicators in this paper; GRD images have no advantage in terms of data richness. Although the data volume of SLC images is four times that of GRD images, downloading SLC images using IDM (Internet download manager) software that supports break point resumption can easily avoid this shortcoming. The SVM machine-learning method used in this paper not only adopts the basis of the change detection method, but also supplements other avalanche scattering and interference characteristics as a basis for identifying avalanches comprehensively. Therefore, it is more complete in principle and more rigorous in logic, and the classification problem is simplified. Thus, classification

accuracy of this method is higher and more objective, affording wider applicability. Further, the ability to identify small avalanches and those in complex terrain and unfavorable atmospheric conditions is superior.

Many studies have interpreted avalanches based on their tongue shape. The results of this study indicate that the tongue shape is more pronounced on hillsides with broad slopes and simple underlying surfaces, but there are other shapes caused by the terrain. For example, avalanches that occur in fjords generally appear as narrow strips in the starting area. A fan shape will appear in the jumping area and the accumulation area when there is enough release space. In complex areas with steep terrain and large undulations, some avalanche shapes are “S” and some are “Z”. In short, the forms are diverse. The research in this paper updates the description of avalanche geometry and perfects the basis for visual interpretation of avalanches.

5.3. Sources of Error

The SVM does not require a large number of samples and does not have the problems of learning and dimensional disasters. Its advantages make the accuracy of classification results higher. Although the number of mixed pixels in the sample is controlled as artificially as possible, the establishment of indicators using polarization decomposition and the automatic avalanche identification by SVM are essentially pixel-based image classification technologies; inevitably, the phenomenon of “different objects with the same spectrum” exists. For example, bodies of water and avalanches have repetitive backscatter and coherence coefficient values. This investigation found that flowing unfrozen water was the main cause of the increase σ in water body. Water is an extremely unstable scatterer. The change in the water phase is the main reason for weak coherence [47]. The $\Delta\sigma$ and γ indicators of water bodies and avalanches are similar, but clearly separable in the ΔH and $\Delta\alpha$ indicators. In addition, it is easier to avoid misjudgments in water bodies. Water bodies, coniferous forests, roads and avalanches have similar numeric intervals in some indicators and cause some interference with the automatic identification of avalanche but coordinating with all indicators can lesson misjudgment.

The phenomenon of “same object with a different spectrum” can be caused by natural changes of seasonal snow, the complex dynamic changes in the snow layer and its interaction with the soil below and the air above. For example, wind-blown snow has a rough surface similar to that of an avalanche, produces similar changes in backscatter, which restricts the distinguishing performance of indicators. Other special ground cover conditions can be additional sources of error. For example, the C-band receives echoes from the canopy in most cases; features hidden among dense forests can also be detected at certain small angles. The radar echo received in that case is more complicated and may cause misjudgment. Some avalanches are obscured by intertwined branches and leaves, and radar cannot receive echoes from the avalanche, resulting in errors of omission.

5.4. Limitations and Future Development

Accuracy can be limited by the resolution of the Sentinel-1 image, the penetrating power of the C-band, shadows in the image and the phenomenon of overlapping and shortening on slopes. Smaller avalanches can be identified using Sentinel-1 images due to its higher spatial resolution, but very small avalanches will still be missed. Penetrating dry snow in the Sentinel-1 C-band would further increase omissions, resulting in a reduction of accuracy. Sentinel-1 is a side-look radar, in a hilly area where the terrain is undulating and steep, shadows are generated on the side facing away from the radar, and the signal cannot be received.

Automatic avalanche monitoring research is in the development and exploration stage. Because Sentinel-1 data are available worldwide, this method is applicable in the most mountainous areas of the world that are affected by avalanches. It is hoped that this study will provide reference and inspiration for subsequent research. Replacing source data with more perfect performance data could be considered in future improvements. The use of high-resolution images to enhance the detection of small avalanches is of great significance for the management and control of potential avalanche disasters.

Different polarizations can reflect varying characteristics between ground objects and electromagnetic waves. However, at present, only dual-polarization (VV–VH) images are used primarily. These are more conducive to a comprehensive and in-depth analysis of the characteristics of the ground objects using fully polarized images containing all the scattering information of ground objects. Furthermore, the band of radar used to detect avalanches renders vital knowledge. Considering the influence of the atmospheric transmission window, frequency and polarization on information extraction, the L, C and X bands are more suitable. They can all be used to detect snow accumulation. Regardless of horizontal or vertical polarization, the C-band penetrates to a certain depth of the dry snow layer, which often leads to missed dry snow avalanches. Therefore, the advantages of X- and L-band SAR images in automatic identification of avalanches are worth exploring. Subsequently, important information, such as avalanche morphology, texture and albedo, can be clearly characterized by high-quality optical images. Using fused multi-source remote sensing images can greatly improve the accuracy of avalanche detection. In terms of method improvement, increasing indicators such as snow depth and avalanche flow direction is suggested to make the model more complete. This was not done in this case to avoid introducing errors, because the method of inverting these two indicators is not fully developed. As for expanding on the research content, following up and exploring the changes of avalanches in the context of climate change, long-term series, and the impact of avalanches on landform and ecological patterns are proposed.

6. Conclusions

This study proposes for the first time a robust and universal method to automatically detect regional avalanches using scattering and interference information from active microwave C-band images, which can generate more objective and accurate avalanche maps—especially while descending. The results of this study carried out in two mountainous areas of western TianShan show that avalanches are unevenly distributed in space, but mainly concentrated at 1600–3500 m above sea level and on 25° to 35° slopes and that most of them are small-scale. Avalanches along G217 and G218, that are adjacent to human activities are extremely active and should be given urgent attention to mitigate possible losses in advance.

The excellent performance of this method is manifested in its objectivity, universal applicability and automation, allowing avalanche mapping unhindered by extreme geographical conditions, coarse image quality and artificial subjective experience. The realization of rapid and automatic detection of regional avalanches has profound social significance, which can assist in dealing with the threat of destructive natural disasters from avalanche and improve public awareness of the danger.

Author Contributions: J.Y. and Y.L. provided and designed the auto-detection idea; J.Y., Y.L. and T.H. designed and implemented the avalanche survey; L.L. provided meteorological and historical avalanche data; J.Y. and Y.L. analyzed the results; J.Y. wrote the initial paper, L.L., J.D., C.L. and R.Z. reviewed the manuscript and gave suggestions for revision. All authors have read and agreed to the published version of the manuscript.

Funding: This study was supported by the National Natural Science Foundation of China (NSFC Grant 41901087) and the West Light Foundation of the Chinese Academy of Sciences (No. 2018-XBQNZ-B-012).

Acknowledgments: The authors would like to thank L.L., C.L., Y.L., R.Z. and T.H. for the support in providing data and linguistic assistance. We are especially grateful to the anonymous reviewers and editors for appraising our manuscript and for offering instructive comments.

Conflicts of Interest: The authors declare no conflict of interest.

References

1. Ballesteros-Cánovas, J.A.; Trappmann, D.; Madrigal-González, J.; Eckert, N.; Stoffel, M. Climate warming enhances snow avalanche risk in the Western Himalayas. *Proc. Natl. Acad. Sci. USA* **2018**, *115*, 3410–3415. [[CrossRef](#)] [[PubMed](#)]
2. Grêt-Regamey, A.; Straub, D. Spatially explicit avalanche risk assessment linking Bayesian networks to a GIS. *Nat. Hazards Earth Syst. Sci.* **2006**, *6*, 911–926. [[CrossRef](#)]

3. Blahut, J.; Klimeš, J.; Balek, J.; Hájek, P.; Červená, L.; Lysák, J. Snow avalanche hazard of the Krkonose National Park, Czech Republic. *J. Maps* **2017**, *13*, 86–90. [[CrossRef](#)]
4. Krajick, K. Animals thrive in an avalanche's wake. *Science* **1998**, *279*, 1853. [[CrossRef](#)]
5. Gruber, U.; Bartelt, P. Snow avalanche hazard modelling of large areas using shallow water numerical methods and GIS. *Environ. Model. Softw.* **2007**, *22*, 1472–1481. [[CrossRef](#)]
6. Gądek, B.; Kaczka, R.J.; Rączkowska, Z.; Rojan, E.; Casteller, A.; Bebi, P. Snow avalanche activity in Żleb Żandarmerii in a time of climate change (Tatra Mts., Poland). *Catena* **2017**, *158*, 201–212. [[CrossRef](#)]
7. Bernardino, C.; Valerio, D.B.; Barbara, F. The influence of extreme snowfall on snow avalanche impact pressure. *Contrib. Polit. Econ.* **2013**, *28*, 1–22.
8. Rudolf, M.F.; Sauermoser, S.; Mears, A.I. *The Technical Avalanche Protection Handbook*; Ernst & Sohn: Berlin, Germany, 2015; pp. 93–127.
9. Germain, D. Snow avalanche hazard assessment and risk management in northern Quebec, eastern Canada. *Nat. Hazards* **2015**, *80*, 1303–1321. [[CrossRef](#)]
10. Gaume, J.; Herwijnen, A.V.; Chambon, G.; Wever, N.; Schweizer, J. Snow fracture in relation to slab avalanche release: Critical state for the onset of crack propagation. *Cryosphere* **2017**, *11*, 217–228. [[CrossRef](#)]
11. Eckerstorfer, M.; Malnes, E. Manual detection of snow avalanche debris using high-resolution Radarsat-2 SAR images. *Cold Reg. Sci. Technol.* **2015**, *120*, 205–218. [[CrossRef](#)]
12. Singh, D.K.; Mishra, V.D.; Gusain, H.S.; Gupta, N.; Singh, A.K. Geo-spatial modeling for automated demarcation of snow avalanche hazard areas using Landsat-8 satellite images and in situ data. *J. Indian Soc. Remote Sens.* **2019**, *47*, 513–526. [[CrossRef](#)]
13. Bedard, A.J. Low-frequency sound waves associated with avalanches, atmospheric turbulence, severe weather, and earthquakes. *J. Acoust. Soc. Am.* **1998**, *94*, 1872. [[CrossRef](#)]
14. Chadha, A.; Satam, N. Snow Avalanche: Study and detection using remote sensing techniques. *Int. J. Recent Trends Eng. Res.* **2017**, *3*, 11–23.
15. Luckman, B.H. Drop stones resulting from snow avalanche deposition on lake ice. *J. Glaciol.* **1975**, *70*, 186–188. [[CrossRef](#)]
16. D'Aubeterre, G.D.B.; Favillier, A.; Mainieri, R.; Lopez, S.J.; Eckert, N.; Saulnier, M.; Peiry, J.L.; Stoffel, M.; Corona, C. Tree-ring reconstruction of snow avalanche activity: Does avalanche path selection matter? *Sci. Total Environ.* **2019**, *684*, 496–508.
17. Bühler, Y.; Hafner, E.; Zweifel, B.; Zesiger, M.; Heisig, H. Where are the avalanches? Rapid mapping of a large snow avalanche period with optical satellites. *Cryosph. Discuss.* **2019**, 119. [[CrossRef](#)]
18. Lato, M.J.; Frauenfelder, R.; Bühler, Y. Automated detection of snow avalanche deposits: Segmentation and classification of optical remote sensing imagery. *Nat. Hazards Earth Syst. Sci.* **2012**, *12*, 2893–2906. [[CrossRef](#)]
19. Wiesmann, A.; Wegmuller, U.; Honikel, M.; Strozzi, T.; Werner, C. Potential and methodology of satellite based SAR for hazard mapping. In Proceedings of the IEEE International Geoscience & Remote Sensing Symposium, Sydney, Australia, 9–13 July 2001.
20. Eckerstorfer, M.; Vickers, H.; Malnes, E. Snow avalanche activity monitoring from space: Creating a complete avalanche activity dataset for a Norwegian forecasting region. In Proceedings of the International Snow Science Workshop, Breckenridge, CO, USA, 3–7 October 2016.
21. Benz, U.; Baatz, M.; Schreier, G. OSCAR object oriented segmentation and classification of advanced radar allow automated information extraction. In Proceedings of the IEEE International Geoscience & Remote Sensing Symposium, Sydney, Australia, 9–13 July 2001.
22. Malnes, E.; Eckerstorfer, M.; Vickers, H. First Sentinel-1 detections of avalanche debris. *Cryosph. Discuss.* **2015**, *9*, 1943–1963. [[CrossRef](#)]
23. Eckerstorfer, M.; Malnes, E.; Frauenfelder, R.; Domass, U.; Brattlien, K. Avalanche debris detection using satellite-borne radar and optical remote sensing. In Proceedings of the International Snow Science Workshop, Banff, AB, Canada, 29 September–3 October 2014.
24. Eckerstorfer, M.; Malnes, E.; Müller, K. A complete snow avalanche activity record from a Norwegian forecasting region using Sentinel-1 satellite-radar data. *Cold Reg. Sci. Technol.* **2017**, *8*, 39–51. [[CrossRef](#)]
25. Singh, A.; Ganju, A. Artificial Neural Networks for snow avalanche forecasting in Indian Himalaya. In Proceedings of the 12th International Conference of International Association for Computer Methods and Advances in Geomechanics (IACMAG), Goa, India, 1–6 October 2008.

26. Möhle, S.; Bründl, M.; Beierle, C. Modeling a system for decision support in snow avalanche warning using balanced random forest and weighted random forest. *Bioinform. Res. Appl.* **2014**, *8722*, 80–91.
27. Rahmati, O.; Ghorbanzadeh, O.; Teimurian, T.; Mohammadi, F.; Tiefenbacher, J.P.; Falah, F.; Pirasteh, S.; Ngo, P.T.T.; Bui, D.T. Spatial modeling of snow avalanche using machine learning models and geo-environmental factors: Comparison of effectiveness in two mountain regions. *Remote Sens.* **2019**, *11*, 2995. [[CrossRef](#)]
28. Abake, G.; Al-Hanbali, A.; Alsaadeh, B. Potential hazard map for snow disaster prevention using GIS-based weighted linear combination analysis and remote sensing techniques: A case study in Northern Xinjiang, China. *Adv. Remote Sens.* **2014**, *3*, 260–271. [[CrossRef](#)]
29. Qiu, J.Q. *Avalanche*; Xinjiang Science and Technology Press: Urumqi, China, 2004; pp. 182–186.
30. Osamu, A.; Li, L.H.; Bai, L.; Hao, J.S.; Hirashima, H.; Xu, J.R. Characteristics of avalanche release and an approach of avalanche forecasting system using SNOW PACK model in the Tianshan mountains, China. In Proceedings of the International Snow Science Workshop, Breckenridge, CO, USA, 2 October 2016.
31. Hao, J.H.; Huang, F.R.; Liu, Y.; Amanambu, A.C.; Li, L.H. Avalanche activity and characteristics of its triggering factors in the western Tianshan Mountains, China. *J. Mt. Sci.* **2018**, *15*, 1397–1411. [[CrossRef](#)]
32. Liu, D.X.; Cheng, Z.L.; Zhao, X.; Huang, J.H.; Liu, J.K. Research and application status of avalanche prevention and control engineering. *J. Mt.* **2013**, *31*, 425–433.
33. Heffernan, O. Coming down the tracks. *Nat. Clim. Chang.* **2018**, *8*, 937–939. [[CrossRef](#)]
34. Banque, X.; Lopez Sanchez, J.M.; Monells, D.; Ballester, D.; Duro, J.; Koudogbo, F. Polarimetry based land cover classification with Sentinel-1 data. In Proceedings of the PolInSAR 2015, Frascati, Italy, 26–30 January 2015.
35. Xie, Q.X.; Meng, Q.Y.; Zhang, L.L.; Wang, C.M.; Wang, Q.; Zhao, S.H. Combining of the H/A/Alpha and Freeman–Durden polarization decomposition methods for soil moisture retrieval from full-polarization Radarsat-2 data. *Adv. Meteorol.* **2018**, *2018*, 9436438. [[CrossRef](#)]
36. Ulaby, F.T.; Moore, R.K.; Funk, A.K. *Microwave Remote Sensing, Active and Passive: From Theory to Applications*; Artech House: Norwood, MA, USA, 1986; pp. 2026–2086.
37. Li, Z.; Guo, H.D.; Li, X.W.; Wang, C.L. SAR interferometry coherence analysis and snow mapping. *J. Remote Sens.* **2002**, *6*, 334–338.
38. Tanase, M.A.; Santoro, M.; Wegmüller, U. Properties of X, C and L-band repeat pass interferometric SAR coherence in Mediterranean pine forests affected by fires. *Remote Sens. Environ.* **2010**, *114*, 2182–2194. [[CrossRef](#)]
39. Clark, N.R.; Ma’Ayan, A. Introduction to statistical methods to analyze large data sets: Principal Components Analysis. *Sci. Signal.* **2011**, *4*. [[CrossRef](#)]
40. Tripathi, M.; Singal, S.K. Use of Principal Component Analysis for parameter selection for development of a novel Water Quality Index: A case study of river Ganga India. *Ecol. Indic.* **2019**, *96*, 430–436. [[CrossRef](#)]
41. Li, F.; Huang, J.H.; Zeng, G.M.; Yuan, X.Z.; Li, X.D.; Liang, J.; Wang, X.Y.; Tang, X.J.; Bai, B. Spatial risk assessment and sources identification of heavy metals in surface sediments from the Dongting Lake, Middle China. *J. Geochem. Explor.* **2013**, *132*, 75–83. [[CrossRef](#)]
42. Xiao, M.H.; Ma, Y.; Feng, Z.X.; Deng, Z.; Hou, S.S.; Shu, L.; Lu, Z.X. Rice blast recognition based on principal component analysis and neural network. *Comput. Electron. Agric.* **2018**, *154*, 482–490. [[CrossRef](#)]
43. Chauhan, V.K.; Dahiya, K.; Sharma, A. Problem formulations and solvers in linear SVM: A review. *Artif. Intell. Rev.* **2018**, *52*, 803–855. [[CrossRef](#)]
44. Marjanovic, M.; KovacEvic, M.; Bajat, B.; Voženilek, V. Landslide susceptibility assessment using SVM machine learning algorithm. *Eng. Geol.* **2011**, *123*, 225–234. [[CrossRef](#)]
45. Alham, N.K.; Li, M.; Liu, Y.; Ponraj, M.; Qi, M. A distributed SVM ensemble for image classification and annotation. In Proceedings of the 9th International Conference on Fuzzy Systems and Knowledge Discovery, SiChuan, China, 29–31 May 2012.
46. Wesselink, D.S.; Malnes, E.; Eckerstorfer, M.; Lindenbergh, R.C. Automatic detection of snow avalanche debris in central Svalbard using C-band SAR data. *Polar Res.* **2017**, *36*. [[CrossRef](#)]

47. Eckerstorfer, M.; Vickers, H.; Malnes, E.; Grahn, J. Near-Real time automatic snow avalanche activity monitoring system using Sentinel-1 SAR data in Norway. *Remote Sens.* **2019**, *11*, 2863. [[CrossRef](#)]
48. Korzeniowska, K.; Bühler, Y.; Marty, M.; Korup, O. Regional snow avalanche detection using object-based image analysis of near-infrared aerial imagery. *Nat. Hazards Earth Syst. Sci.* **2017**, *17*, 1823–1836. [[CrossRef](#)]
49. Vickers, H.; Eckerstorfer, M.; Malnes, E.; Larsen, Y.; Hindberg, H. A method for automated snow avalanche debris detection through use of Synthetic Aperture Radar (SAR) imaging: Automated avalanche detection. *Earth Space Sci.* **2016**, *3*, 446–462. [[CrossRef](#)]



© 2020 by the authors. Licensee MDPI, Basel, Switzerland. This article is an open access article distributed under the terms and conditions of the Creative Commons Attribution (CC BY) license (<http://creativecommons.org/licenses/by/4.0/>).